



HAL
open science

200 mm-scale growth of 2D layered GaSe with preferential orientation

Mickaël Martin, Pascal Pochet, Hanako Okuno, Carlos Alvarez, Edith Bellet-Amalric, Pauline Hauchecorne, Théo Levert, Bernard Pelissier, Łukasz Borowik, Franck Bassani, et al.

► **To cite this version:**

Mickaël Martin, Pascal Pochet, Hanako Okuno, Carlos Alvarez, Edith Bellet-Amalric, et al.. 200 mm-scale growth of 2D layered GaSe with preferential orientation. *APL Materials*, 2022, 10 (5), pp.051106. 10.1063/5.0087684 . hal-03694297

HAL Id: hal-03694297

<https://hal.science/hal-03694297v1>

Submitted on 23 Sep 2024

HAL is a multi-disciplinary open access archive for the deposit and dissemination of scientific research documents, whether they are published or not. The documents may come from teaching and research institutions in France or abroad, or from public or private research centers.







L'archive ouverte pluridisciplinaire **HAL**, est destinée au dépôt et à la diffusion de documents scientifiques de niveau recherche, publiés ou non, émanant des établissements d'enseignement et de recherche français ou étrangers, des laboratoires publics ou privés.



Distributed under a Creative Commons Attribution 4.0 International License

RESEARCH ARTICLE | MAY 09 2022

200 mm-scale growth of 2D layered GaSe with preferential orientation

Mickaël Martin; Pascal Pochet ; Hanako Okuno; Carlos Alvarez; Edith Bellet-Amalric ; Pauline Hauchecorne; Théo Levert; Bernard Pelissier; Łukasz Borowik ; Franck Bassani ; Sylvain David; Jeremy Moeyaert; Thierry Baron  



APL Mater. 10, 051106 (2022)
<https://doi.org/10.1063/5.0087684>



APL Quantum
Latest Articles Now Online
Read Now



200 mm-scale growth of 2D layered GaSe with preferential orientation

Cite as: APL Mater. 10, 051106 (2022); doi: 10.1063/5.0087684

Submitted: 8 February 2022 • Accepted: 19 April 2022 •

Published Online: 9 May 2022








View Online



Export Citation



CrossMark

Mickaël Martin,¹ Pascal Pochet,²  Hanako Okuno,² Carlos Alvarez,² Edith Bellet-Amalric,³  Pauline Hauchecorne,^{1,4} Théo Levert,¹ Bernard Pelissier,¹ Łukasz Borowik,⁴  Franck Bassani,¹  Sylvain David,¹ Jeremy Moeyaert,¹ and Thierry Baron^{1,a)} 

AFFILIATIONS

¹University Grenoble Alpes, CNRS, CEA/LETI Minatec, Grenoble INP, LTM, 38000 Grenoble, France

²University Grenoble Alpes, CEA, IRIG, Department of Physics, 38000 Grenoble, France

³University Grenoble Alpes, CEA, Grenoble INP, IRIG, PHELIQS, 38000 Grenoble, France

⁴University Grenoble Alpes, CEA, LETI, 38000 Grenoble, France

^{a)} Author to whom correspondence should be addressed: thierry.baron@cea.fr

ABSTRACT

In this article, we present a fab-compatible metal–organic chemical vapor deposition growth process, realized in a hydrogen ambience, of two-dimensional (2D) layered GaSe on 200 mm diameter Si(111) wafers. Atomic scale characterization reveals initial stages of growth consisting of passivation of the H–Si (111) surface by a half-monolayer of GaSe, followed by nucleation of 2D-GaSe from the screw dislocations located at the step edges of the substrate. We, thus, demonstrate that by using a Si wafer that is slightly misoriented toward $[\bar{1}\bar{1}2]$, the crystallographic orientation of 2D-GaSe can be step-edge-guided. It results in a coalesced layer that is nearly free from antiphase boundaries. In addition, we propose a sequential process to reduce the density of screw dislocations. This process consists in a subsequent regrowth after partial sublimation of the initially grown GaSe film. The local band bending in GaSe near the antiphase boundaries measured by Kelvin probe force microscopy emphasizes the electrical activity of these defects and the usefulness of having a nearly single-orientation film. Such a low defectivity layer opens up the way toward large-scale integration of 2D-optical transceivers in Si CMOS technology.

© 2022 Author(s). All article content, except where otherwise noted, is licensed under a Creative Commons Attribution (CC BY) license (<http://creativecommons.org/licenses/by/4.0/>). <https://doi.org/10.1063/5.0087684>

I. INTRODUCTION

Discovery of graphene and its ultra-high electron mobility¹ has resulted in huge research activity on the singular properties of atomically thin materials. In particular, two-dimensional materials with non-zero bandgaps have attracted considerable interest owing to their integration capability in digital and optoelectronic components. Among them, transition metal dichalcogenides (TMDs) are now probably the most studied family of 2D materials “beyond graphene”.² TMDs, with a generalized formula of MX_2 ($M = Mo, W, \dots$; $X = Se, S, Te$), have already demonstrated good potential for novel applications in electronics,³ optoelectronics,⁴ spin and valleytronics,⁵ etc. However, most of the interesting properties of TMDs only arise at thicknesses on the scale of an atomic monolayer (ML). In particular, a few-layer film induces a direct-to-indirect bandgap crossover. Bandgap energy tuning by quantum confinement (layer stacking) thereby offers a very restricted capacity

to change the spectral emission range of these materials. Furthermore, synthesis and integration of a single layer over a wide area remain very challenging to control in terms of the fabrication process. Alternatively, group III–VI compounds, MX ($M = Ga, In$; $X = S, Se, Te$), represent an attractive emerging class of 2D layered materials possessing desirable optical and electrical properties as well as direct bandgaps for few-nanosheets. As a member of the III–VI group, the 2D-GaSe layer consists of four covalently bonded atomic planes Se–Ga–Ga–Se with a D_{3h} symmetry. The lattice constant in the hexagonal basal plane is $a = b = 0.375$ nm. GaSe has already widely been used to demonstrate solar cells,^{6,7} fast response photodetectors on rigid^{8–13} and flexible substrates,^{14,15} light emitters,^{16–18} large second harmonic generation,^{19,20} and terahertz sources.^{21,22}

Nevertheless, as for all 2D materials, the integration of III–VI for industrial applications will only be possible if a large-scale fabrication method of a *single-crystal* can be achieved. In addition,

for a large number of applications, which require the integration with CMOS circuits (logic components, RF, resistive RAM, photodetectors, light emitters, etc.), the process must be fully compatible with Si-based technology. However, aside from the mechanical and liquid exfoliation,^{12,13,23} pulsed laser deposition,²⁴ molecular beam epitaxy,^{10,25–27} and powder vaporization,^{7,9,25,28–30} there are currently few reports on fab-compatible growth techniques of 2D materials such as metal organic chemical vapor deposition (MOCVD). To the best of our knowledge, all of them are dedicated to TMDs and hBN growth and there is still none on the III–VI materials. Thus, significant results were already shown for MOCVD growth of WSe₂-on-sapphire,^{31–34} MoS₂-on-SiO₂,^{35,36} hBN-on-sapphire, and –Ni(111).^{37–39} Nevertheless, the methodology for 2D growth is still in its infancy as many challenges remain, such as carbon contamination originating from precursors,⁴⁰ high density of metal-rich aggregates,^{31,41} unwanted multilayer growth,⁴² use of incompatible (or expensive) substrates in a fab environment,³⁷ excessive growth time,^{35,36} or chalcogenide precursors consumption.³² Above all, and whatever the growth method, rotational domain (RDs) formation remains a critical issue in 2D materials growth even when an epitaxial relationship with the substrate can be achieved.^{25–27,43–45} The real influence of RDs and grain boundaries (GBs) on electrical transport and optical properties has not yet been addressed in the literature for the III–VI compounds. Nevertheless, a large number of research studies on graphene and TMDs have already emphasized the detrimental effects that GBs can have on the transport and/or optical properties of the material.^{46–48} The growth of a single-oriented 2D layer is a complex issue since RDs can be generated by multiple factors such as symmetry, commensurability, and interaction with substrate. Several years ago, an innovative approach was shown to overcome this hurdle by using step-edge-guided nucleation of WSe₂-on-sapphire,⁴⁹ even though the mechanisms involved and the required substrate specifications were not investigated in detail. More recently, experimental⁵⁰ and theoretical⁵¹ reports have demonstrated the feasibility of a large hBN single-crystal grown on a copper-foil with a similar method. In these reports, the hBN-monolayer orientation is directly driven by the step edges direction of the Cu(110) substrate. Nevertheless, these first demonstrations are still limited by the usage of substrates incompatible with Si-CMOS integration. GaSe is an interesting candidate for combining both the step-edge guided growth approach and Si-CMOS compatible wafers. Indeed, seminal studies have already highlighted the electronic passivation of the Si(111) substrate by a Ga–Se half-monolayer termination.^{52–55} This highly stable and weakly strained GaSe half monolayer (~2% of lattice mismatch with Si) is very suitable for a subsequent van der Waals epitaxy.^{56,57}

In this work, we propose a multi-step MOCVD growth method of 2D-GaSe on 200 mm-scale Si(111) wafers that is fully compatible

with the CMOS platform. We show that the first GaSe monolayer nucleates by covalent bonding with the step-edges of the substrate. The screw dislocations induced by this mechanism in the first monolayer are responsible for directing the growth of subsequent GaSe layers. Thus, by using a Si(111) substrate with step-edges oriented in the $\langle 11\bar{2} \rangle$ direction, we demonstrate a 2D-GaSe crystal that is mainly single-oriented.

II. EXPERIMENTAL DETAILS

Substrates used were standard 200 mm diameter Czochralsky (CZ)-grown Si(111) wafers, sliced from the ingot with a slight 0.1–0.2° miscut angle (terrace width ~100 to 200 nm). The step edges of the substrates were oriented in the main directions of the Si(111) surface, i.e., either along the $\langle 110 \rangle$ direction: **substrate No. 1** or in the $\langle 1\bar{1}2 \rangle$ direction: **substrate No. 2**. Deoxidization was performed in a SiConiTM chamber using a NF₃/NH₃ remote plasma. The wafers were then transferred into the MOCVD chamber for H₂ annealing at 900 °C/600Torr to realize smooth Si(111)–H (1 × 1) terraces with well aligned step edges under N₂ ambience.⁵⁸ GaSe layers were grown in a 300 mm Applied Materials MOCVD reactor using a laminar flux of H₂ as the carrier gas, trimethylgallium (TMGa) as the group-III precursor, and diisopropylselenide (DiPSe) as the group-VI precursor. The VI/III ratio was maintained in a range to avoid gallium droplet formation at a ratio of <4 or selenide droplets at a ratio of >7. The baseline process consists of two stages. (1) First, a nucleation step is carried out. Both the substrate passivation layer and the GaSe nuclei are achieved quasi-simultaneously in this step. Typically, with the OM precursors used, this first step is performed in the 500–550 °C range. (2) Next, a step of lateral growth of the nuclei is performed at very low partial pressure ($P_{\text{TMGa}} \sim 10^{-3}$ Torr) and high temperature (>600 °C) to promote long-range adatom surface diffusion. In this growth regime, the supersaturation of the precursors is low enough to prevent reaching the critical radius of energetically stable nuclei. Therefore, there is no new nucleus formation in this step and the growth is a purely lateral extension of the preexisting nuclei. To simplify the understanding of the growth process, [Table I](#) summarize the recipe steps.

Surface morphology of the layers was investigated using a Bruker Dimension Icon atomic force microscope (AFM) in a soft-tapping mode using VTESPA-300 tips. Kelvin probe force microscopic (KPFM) measurements were carried out in a UHV (<10⁻¹⁰ Torr) instrument composed of an Omicron Nanotechnology VT-AFM system with a Nanonis controller from SPECS Zurich using AD-2.8-SS tips. Here, fundamental resonant frequency $f_0 = 49.7$ kHz was mechanically excited to control the tip-surface distance by non-contact atomic force microscopy (nc-AFM) with

TABLE I. Baseline process description.

	Recipe steps	T (°C)	P_{TMGa} (Torr)	Time	VI/III
0	H ₂ annealing of the Si(111) substrate	900	...	600 s	...
1	Passivation with $\frac{1}{2}$ GaSe ML + GaSe nucleation	550	$\sim 10^{-2}$	Few seconds	~ 5
2	Lateral growth of nuclei	650	$\sim 10^{-3}$	>300 s	~ 5

a frequency shift setpoint equal to -19 Hz. Specifically, for KPFM mode purposes, we used an additional lock-in amplifier (HF2LI from Zurich Instruments), and measurements were carried out in a single pass mode using heterodyne amplitude modulation KPFM (h-KPFM).⁵⁹ In h-KPFM, a bias voltage $V_{ac} = 500$ mV was applied at $f_1 - f_0$ (f_0 and f_1 are the fundamental resonant frequency and its first harmonic, respectively), which generated an electrostatic force at $f_1 = 371.4$ kHz if the cantilever Vdc bias did not match the contact potential difference (CPD). To measure CPD, a feedback loop was introduced to nullify the cantilever oscillation amplitude at f_1 .

In-plane high-resolution x-ray diffraction (HR-XRD) scans were performed using a Rigaku SmartLab X-Ray diffractometer equipped with a $K\beta$ filter. A parallel in-plane collimator with 0.5° resolution was used in both primary and secondary optics.

Scanning transmission electron microscope (STEM) imaging was carried out using a Cs-corrected Thermo Fisher Themis at 200 kV.

X-ray photoelectron spectroscopy (XPS) measurements have been carried out on a customized parallel angle resolved (pARXPS) Theta 300 from Thermo Fisher Scientific operating under ultra-high vacuum conditions (10^{-9} mbar), alongside a monochromized Al $K\alpha_{1,2}$ x-ray source emitting at 1486.6 eV. Parallel angle resolved

spectra were simultaneously collected without any sample tilt and with an incident angle ranging from 23.75 to 76.25° with regard to the sample's surface normal. Wafer transfer from the epitaxy chamber to the XPS tool was carried out using a specific vacuum carrier⁶⁰ (developed by Pfeiffer Vacuum). This procedure fully prevents unintended oxidation of the GaSe film.⁶¹ Nevertheless, a slight remaining contamination by physisorbed carbon can never be completely avoided during wafer storage in the carrier.

III. RESULTS AND DISCUSSION

AFM images in Fig. 1(a) ($4 \times 4 \mu\text{m}^2$) and Fig. 1(b) ($20 \times 20 \mu\text{m}^2$) show the 2D-GaSe layer grown on **substrate No. 1** with 30 s of nucleation (step 1) followed by 400 s of lateral growth (step 2); (cf. Table I). The layer in the background is fully coalesced and perfectly conformal to the stepped topology of the Si surface. The presence of this continuous film is evidenced by the clearly visible grain boundaries on the AFM image [black arrows on Fig. 1(a)]. The step height extracted from the line profile across a hole in the film is about 0.75 nm (~ 1 ml of GaSe). In addition, the atomic resolution cross-sectional high-angle annular dark-field (HAADF)-STEM image in the $(1\bar{1}0)_{\text{Si}}$ plane [Fig. 1(c)] confirms

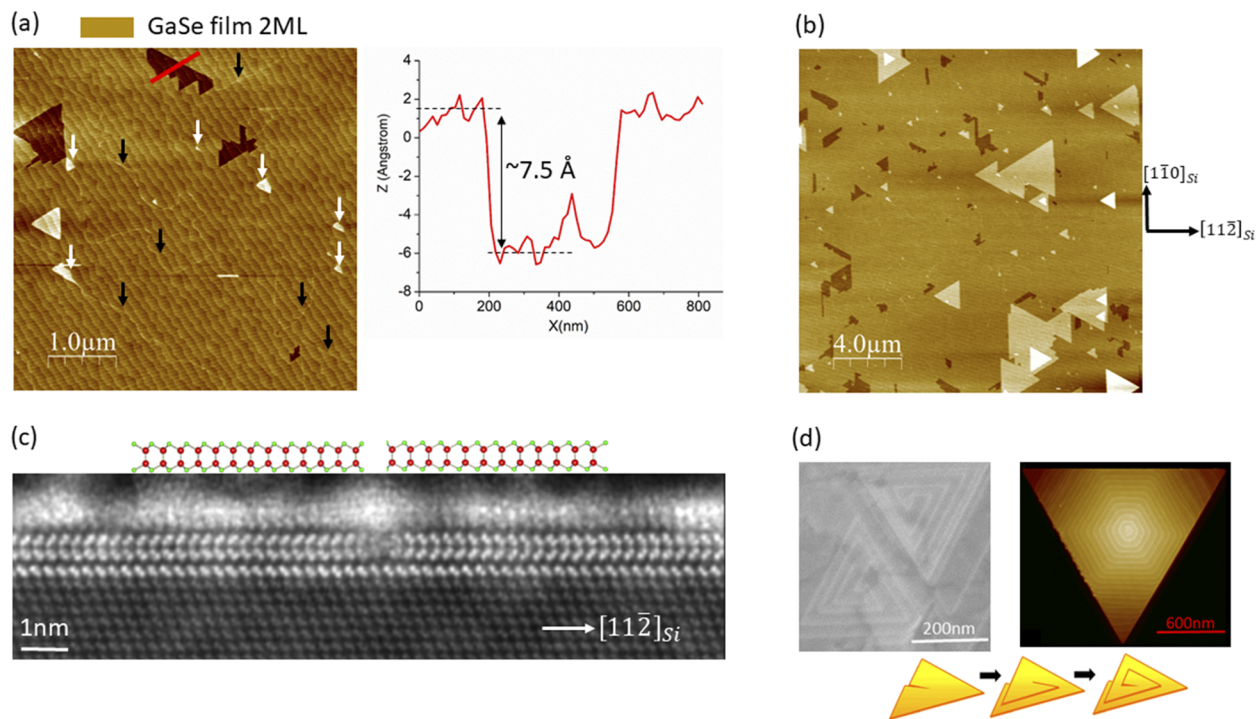


FIG. 1. (a) ($4 \times 4 \mu\text{m}^2$) and (b) ($20 \times 20 \mu\text{m}^2$) AFM images (z-scale 2 nm) of a fully coalesced GaSe film (2 ml)-on-Si(111) with antiphase boundaries (APBs). The edges of the picture correspond to the $[11\bar{2}]$ and $[1\bar{1}0]$ directions of the silicon substrate. APBs and SDs are marked by the black and white arrows, respectively. The step-height extracted from the cross-sectional view (red line on image 1(a)) is about 7.5 \AA (1 ml of GaSe). (c) Cross-sectional HAADF-STEM image of the GaSe film separated by a vdW gap from the Si-Ga-Se interface. Two GaSe-domains, 60° -rotated, are visible on the image. The junction between the two domains (center of the image) form an APB (d) A zooming (SEM and AFM) on the few thick GaSe flakes (>3 ml) of the sample shows a spiral growth mode according to the mechanism depicted on the bottom part of the figure.

the presence of the Ga–Se passivation half-monolayer as well as the 2D-GaSe layer. The latter, cut in the armchair edge, is separated from the passivated substrate by a sharp interface with a typical vdW gap of ~ 0.3 nm. The minimum film thickness is 2 ml on the whole STEM lamella [the second ML in Fig. 1(c) is not clearly visible due to oxidation and lamella preparation]. Nevertheless, several multilayer triangular flakes can be observed on top of the continuous thin film [Fig. 1(b)]. The domain sizes measure up to several microns. Higher magnification of the thickest multilayer flakes provides interesting clues on the growth mode [SEM and AFM images of Fig. 1(d)]. A helical (spiral) stacking morphology is indeed observed. The spiral consists of connected layers with areas that decrease monotonically at each level of the stratified hillock. This growth mode acts in a similar manner to the screw dislocation driven growth (SDD).⁶² In SDD growth, dislocations with a screw component emerge at the surface and create an additional step. The propagation of this step edge by atom addition during growth will then result in a helical trajectory around the vertical Burgers vector of the screw dislocation [cf. scheme Fig. 1(d)]. These screw dislocations (SDs) can also be seen on the coalesced layer in Fig. 1(a) from the reentrant angle of the surface step generated by the emergence of the Burgers vectors (white arrows). Moreover, the AFM image in Fig. 1(a) also suggests a preferential orientation of the GaSe crystal. The triangular flakes appear to be pointing toward the $[11\bar{2}]$ direction of the Si substrate. Nevertheless, opposite 60° -rotational domains (antiphase domains, or APDs) are also present. When these mirror twin domains merge, they are separated by antiphase boundaries (APBs). The antiphase disorder in the 2D-layer can also be observed from the STEM profile view [Fig. 1(c)]. The 60° -rotational domains merge by forming a linear defect perpendicular to the image plane (APB in central part of the figure).

In-plane high-resolution XRD scans were performed in order to precisely measure the epitaxial relationship inferred from the AFM images and STEM cross sections. Figure 2(a) shows the XRD pattern of the in-plane $2\theta_\chi$ scan with the sample aligned on the (110) silicon peak. All diffraction lines are indexed as (hh0) GaSe reflexions. In other words, during the scan, the momentum transfer vector $\Delta\vec{k}$ follows a straight path in the reciprocal space crossing $(110)_{\text{GaSe}}$, $(220)_{\text{GaSe}}$, $(220)_{\text{Si}}$, and $(440)_{\text{Si}}$. This emphasizes an epitaxial relationship with $(110)_{\text{GaSe}} \parallel (110)_{\text{Si}}$. The in-plane lattice parameter extracted from the interplanar spacing is $a = 0,37$ nm, which is in close match with values reported in the literature.

Using $(100)_{\text{GaSe}}$ reflection, the Phi-scan in Fig. 2(b) shows only one variant of GaSe grains, with 60° -periodic peaks due to the hexagonal lattice, although each peak is actually a convolution of the (100) reflections coming from the “up-” and “down-” oriented APDs represented in the inset. Therefore, there are no other rotational domains except the APDs in mirror symmetry along the $[1\bar{1}0]$ direction of silicon.

In order to understand the mechanism triggering the nucleation of a 2D material on industrial-grade, nearly defect-free, silicon wafers, we focused on the very first stages of the growth process. For this purpose, the AFM image in Fig. 3(a) was performed on a Si(111) surface after a few tens of seconds of GaSe nucleation (i.e., step 1 only) on substrate No. 1. First, the growth of the initial GaSe monolayer is slightly anisotropic (white arrows); the elongated domains roughly follow the shape of the substrate terraces. This observation is consistent with the presence of an Ehrlich–Schwoebel

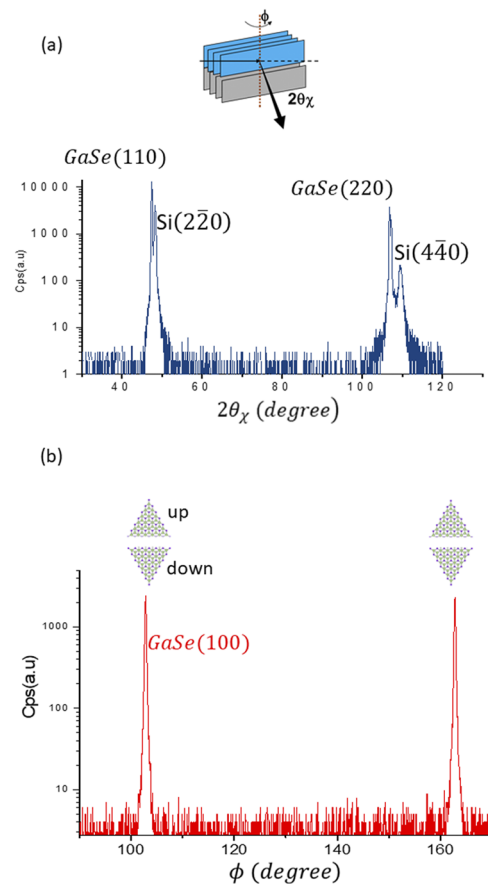


FIG. 2. (a) In-plane $2\theta_\chi$ XRD pattern of GaSe. The scan-angles nomenclature is defined on the schemes (c) 60° -periodic φ -scan from the $(100)_{\text{GaSe}}$ reflection. The inset drawing shows the “up-” and “down-” domains corresponding to the diffraction peaks.

barrier^{63,64} to the diffusion at the step edges. The growth rate of the first GaSe monolayer will be, thus, faster in the direction parallel to the substrate terraces than in the perpendicular direction. Then, the second monolayer (and subsequent layers; blue arrows on the image) nucleates from different sites vertically aligned with the step edges of the substrate. More precisely, the STEM image in Fig. 3(b) shows a first monolayer initiated by covalent bonding with dangling bonds at the step edges of the (passivated) substrate. The image clearly illustrates a screw dislocation formation in the GaSe at the step edge of the substrate. Therefore, there is never pure freestanding nucleation of GaSe on the substrate.

This observation is consistent with the crystal growth theory.⁶⁵ The terraces coated with 1 ml of GaSe (or with a Ga–Se passivation half-monolayer) have a very low surface energy, nearly equivalent to the one of the vdW surface of the GaSe bulk crystal; the binding energy of growth species is, thus, higher at the step edges of the substrate with dangling bonds. Furthermore, due to the helical feature of the >2 ml nuclei, we assume that the second monolayer nucleates on the screw dislocations of the first monolayer. These screw

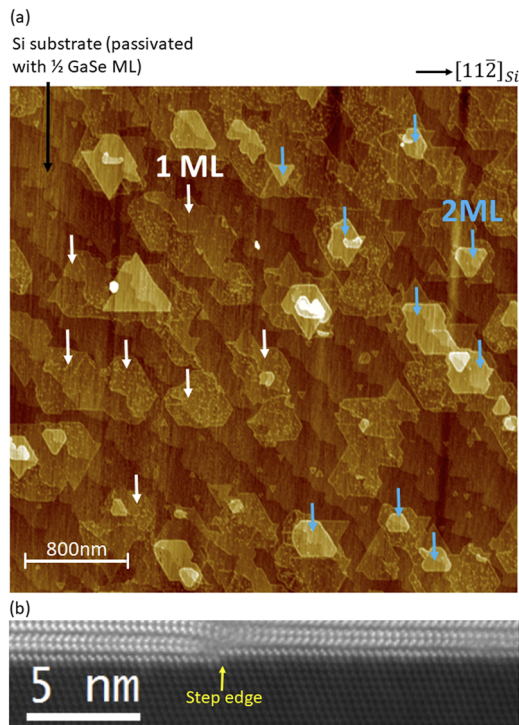


FIG. 3. (a) ($4 \times 4 \mu\text{m}^2$) AFM image (z-scale 3 nm) of the GaSe nanoflakes after a few tens of seconds of the nucleation step. The Si(111) substrate (passivated with Ga–Se half-monolayer termination) is marked by black arrows. The 1 ml and 2 ml-GaSe nuclei are marked by white and blue arrows, respectively. The GaSe nucleation occurs at the step edges of the substrate (b) ($1\bar{1}0$)-cross-sectional view of 2D-GaSe film showing the covalent bond at the substrate step edge and the resulting SD formation.

dislocations are formed by the discontinuity of the first monolayer at the step edges of the substrate.⁵¹ This assumption has important implications. Indeed, in the case of a 2D-layer, the screw dislocation is a zero dimension defect. Thus, by fixing the “polarity” of this 0D defect (i.e., by orienting its dangling bonds), it could be considered to guide the GaSe nucleation. Since the SDs are located at the step edges of the substrate, the step edge direction could be a crucial point for the 2D-layer orientation. There exist two types of steps on the Si(111) surface: monomer steps (monohydride steps in hydrogen ambient) and dimer steps (dihydride steps).^{66–68} Monomer steps are oriented along the $[11\bar{2}]$ direction [or the equivalent $[1\bar{2}1]$, $[\bar{2}11]$ directions due to the threefold symmetry of Si along the $[111]$ -axis], and dimer steps are oriented along the opposite direction $[\bar{1}\bar{1}2]$ (or $[\bar{1}2\bar{1}]$, $[2\bar{1}\bar{1}]$). So far, we have been using Si(111) substrates with two types of step edges (**substrate No. 1** with both monomer and dimer step edges). To know if the polarity of screw dislocations can be fixed, we used **substrate No. 2** with dimer only terminated step edges (with a slight 0.1° miscut angle near the $[\bar{1}\bar{1}2]$ direction). AFM images in Fig. 4 show the surface topography resulting from a GaSe growth on this type of Si substrate. The GaSe triangular flakes, with Se- (or Ga-) terminated zigzag edges,⁶⁹ point to the same direction demonstrating a single-orientation crystal. When compared to substrate No. 1, a majority of the triangular flakes are pointing in the

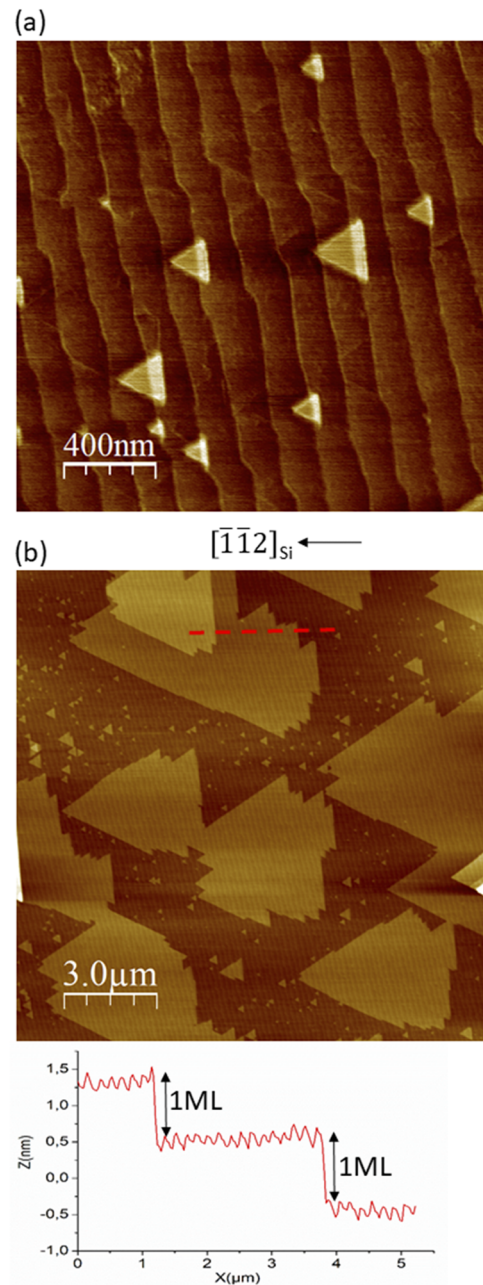


FIG. 4. AFM images at (a) ($2 \times 2 \mu\text{m}^2$) and (b) ($15 \times 15 \mu\text{m}^2$) of 2D-GaSe epitaxy optimized to get a nearly single-orientation (z-scale 2 nm). Most of the triangular flakes are pointing to the left of the image in the substrate (monomer) step edges direction. The height-profile corresponds to the cross-section along the red dotted line in figure (b).

direction of the steps (toward the left side of the image in $[\bar{1}\bar{1}2]_{\text{Si}}$ direction) whatever the observation scale is. It may also be noted that our substrate is not strictly misoriented toward $[\bar{1}\bar{1}2]$ but deviates from ~ 5 to 7° . The very few GaSe nanoflakes arranged in the wrong

orientation can be explained by this offset from the dimer direction. On the other hand, it also demonstrates that the wafer does not need to be sliced from the ingot exactly in the $(\bar{1}\bar{1}\bar{2})$ direction. A shift of several degrees in the miscut direction still allows obtaining a low APBs density. In the context of large-scale fabrication, relaxation of the constraint on the wafer miscut specifications would represent a significant achievement. 2D-GaSe growth on wafers with a vicinal direction too far from the $(\bar{1}\bar{1}\bar{2})$ will lead to APD formation as shown in Fig. 1(a).

The occurrence of GaSe nucleation from the screw dislocations at step edges was pointed out in the previous paragraph. Li *et al.*⁷⁰ demonstrated that GaSe flakes can be reversibly grown or sublimated depending on the process temperature. We drew upon this work to develop a growth-sublimation-regrowth process enabling to decrease the SD density. First, 2 ml of mainly single-oriented GaSe were grown using **substrate No. 2**. Then, the GaSe layer was heated at 710 °C for 2 min to sublimate a part of the layer. In a third step, a fully coalesced bilayer is laterally regrown from the GaSe flakes remaining after step 2. This whole growth-sublimation-regrowth process is repeated three times. The AFM images in Fig. 5(a) show the initial 2 ml-GaSe; with the color scale used, the GaSe film is represented in yellow/orange while the substrate is in dark brown. SDs can be partly observed from the small step edges emerging at the surface of the layer (blue arrows). After 2 min of annealing, about 50% of the layer is sublimated. Both the layer and the enclosed SDs are removed during this step [Fig. 5(b)]. Thus, when GaSe is regrown, the new layer is free of SDs. Indeed, this process step is a pure lateral growth of GaSe and no new nuclei/SDs are formed. Figure 5(c) shows the 2 ml GaSe film after three cycles of growth-sublimation-regrowth. The typical threading step edges induced by SDs are

largely less present although it is difficult to precisely measure their remaining density. From the images, we can roughly estimate the SD density to be 10^6 cm^{-2} , which means ~ 7 times less than without any annealing of the layer. The SD density could probably be further decreased if more than three cycles of growth-sublimation-regrowth were used. However, it was not tested in this study in order to keep a total process time below 90 min. Furthermore, in accordance with the substrate used (**substrate#2**), the layer is mainly single-oriented and the APBs density is low. As already seen before, the APBs have a topological signature and the APB density can be estimated from the images to be $0.07 \mu\text{m}^{-1}$. Table II summarizes the recipe steps of our optimized growth process.

To qualify the capability of our method to grow uniform 2D layers on CMOS compatible substrates, we have measured the thickness uniformity of the GaSe film along the radius of a 200 mm Si(111) wafer by XPS and AFM (in Fig. 6 and Fig. S2 respectively).

For the XPS study, Ga2p, Ga3d, Se3d, Si2p and C1s peaks were measured on a mapping consisting in a five-points line scan along the radius of the wafer. All spectra were collected with angles ranging from 23.75° to 76.25° in order to evaluate the thickness of the GaSe layer. The C peak intensity is in the same range as that for a reference Si substrate, which underwent the same wafer transfer procedure between the growth reactor and the XPS analysis chamber. Therefore, as mentioned in the method section, the carbon contamination is more likely due to the transfer procedure to the XPS tool. The binding energy positions of all mentioned XPS peaks were carefully selected according to reference literature.⁷¹ The spectra were fitted for all angles with the help of the same reference. An example of the resulting fitted data can be found in Fig. S3. First, the resulting data helped us to evaluate the atomic concentration of the main

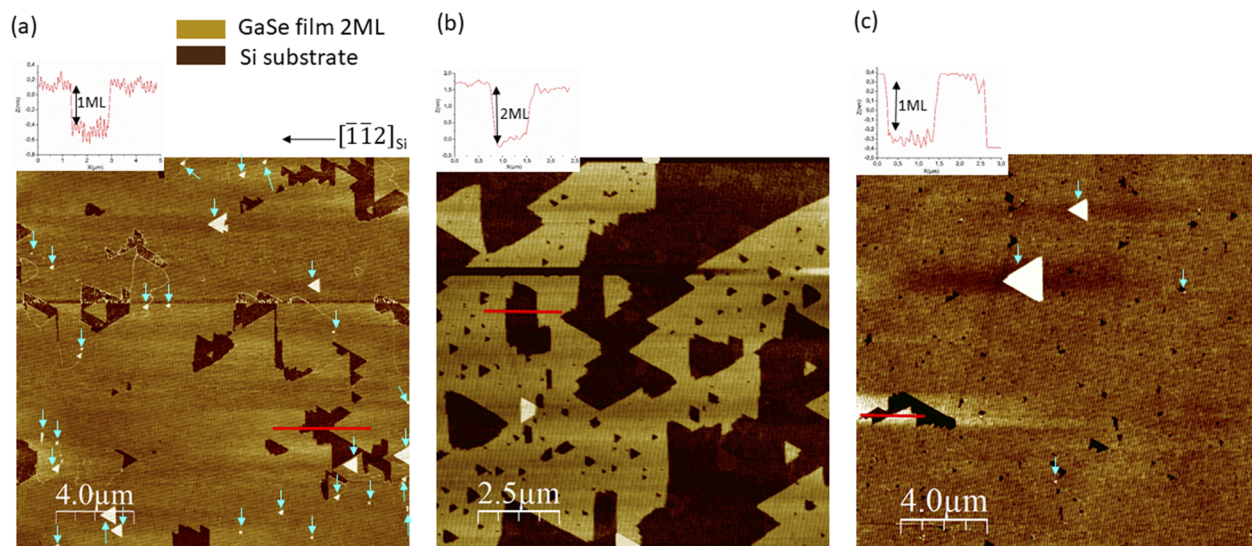
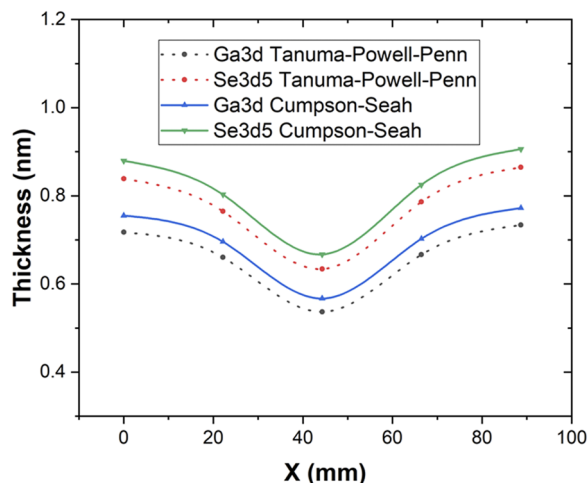


FIG. 5. AFM images (z-scale 2 nm) of the growth-sublimation-regrowth process. The insets represent the height-profile along the red line of the images. The edges of the three images correspond to the $[1\bar{1}\bar{2}]$ and $[\bar{1}\bar{1}0]$ directions: (a) $(20, \times, 20 \mu\text{m}^2)$ image of the initial fully coalesced 2 ml-GaSe film. Blue arrows mark the screw-type threading dislocations. (b) $(12 \times 12 \mu\text{m}^2)$ image of the same layer after 2 min of annealing at 710 °C. About 50% of the GaSe is sublimated. (We used a $12 \mu\text{m}$ scan due to the instability of the AFM tip for larger scan size. In the case of this sublimated layer, the probe is indeed easily contaminated with some GaSe nanoflakes). (c) $(20, \times, 20 \mu\text{m}^2)$ image of the 2 ml GaSe film after three cycles of growth-sublimation-regrowth. The screw-type threading dislocation density is significantly decreased.

TABLE II. Optimized growth process description.

	Recipe steps	T (°C)	P _{TMGa} (Torr)	Time	VI/III
0	H ₂ annealing of Si(111) 0.1°-off → $[\bar{1}\bar{1}2]$	900	...	600 s	...
1	Passivation with $\frac{1}{2}$ GaSe ML + GaSe nucleation	550	$\sim 10^{-2}$	Few seconds	~ 5
2	Lateral growth of nuclei	650	$\sim 10^{-3}$	>300 s	~ 5
3	Partial sublimation of the GaSe film	710	...	120 s	... } × 3
4	Lateral regrowth	650	$\sim 10^{-3}$	>300 s	~ 5

**FIG. 6.** GaSe film thickness, along the radius of the 200 mm wafer, estimated from the XPS models.^{70,71}

species, which can be found in Table III. The Se/Ga ratio, close to the theoretical value of 1, confirms the presence of pure GaSe, while the low standard deviation along the radius validates the uniformity of the GaSe film composition.

The results of the fit were used to evaluate the thickness of the film along the radius, based on both Tanuma–Powell–Penn⁷² and Cumpson–Seah⁷³ methods for the electron mean free paths calculation. The two methods were applied on both Ga3d and Se3d peaks for a better appreciation of the resulting thickness. We can see in Fig. 6 the variation of the evaluated thickness based on different possible configurations and the resulting thickness indicates the presence of a single ML. However, the absolute thickness value

resulting from the calculation is questionable, as it is model-based, and due to the unique character of such 2D material. Thus, AFM and XPS data attest to the presence of the GaSe film overall 200 mm wafer. Nevertheless, a slight non-uniformity in thickness can be observed in mid-radius. This point will be optimized in the future by adjusting the center/edge ratio of gas injection in the MOCVD chamber. In addition, in an absolute value, the GaSe film thickness is about 2 ml with AFM vs 1–1.2 ml with XPS. Such discrepancy could be due to the uncertainty of the model used to fit XPS data. Indeed, the electron mean free paths and attenuation length of the film were evaluated by two methods, based on physical properties of bulk materials,⁷⁴ such as density or bandgap. In the nature of the 2D material, the presence of the Si–Ga–Se interface could introduce a variation from the bulk material properties, affecting the effective mean free path of electrons and, thus, influence the absolute values of the calculated thickness. Despite this discrepancy, a good uniformity of the GaSe film thickness is demonstrated by AFM and XPS on the whole 200 mm Si(111).

We next used this fully coalesced GaSe layer to probe the electrical influence of APBs by UHV-KPFM. To this end, we focused on one of the few APBs on the film. The image in Fig. 7(a) is the surface topography obtained in nc-AFM, while the image in Fig. 7(b) is the surface potential mapping measured using h-KPFM. The silicon substrate (oxidized due to the short air break of the sample) can be observed on the bottom of the hexagonal pits in the GaSe bilayer (white arrows). These small pits correspond to the parts of the GaSe bilayer not completely regrown after the evaporation process step. More interestingly, the contrast of the APBs is visible in both surface topography (yellow arrows) and surface potential imaging. The contact potential difference (V_{CPD}) is measured with a mean value of -280 mV for the 2ml-GaSe at a location far from the defects (value extracted from the distribution in V_{CPD} histogram—not shown here) and at about -160 mV at the APBs location. An example of the measurement is presented

TABLE III. Atomic concentration of the main species.

Point number	X position (mm)	C (at. %)	Si (at. %)	Ga (at. %)	Se (at. %)	Se/Ga ratio (a.u.)
1	0	4.458 07	76.2067	8.927 29	10.407 9	1.165 85
2	22.15	4.427 79	77.7414	8.279 22	9.551 55	1.153 68
3	44.3	3.336 26	82.0249	6.733 32	7.905 54	1.174 09
4	66.45	4.613 27	77.0466	8.383 21	9.956 93	1.187 72
5	88.6663	17.899 3	39.2229	9.107 44	10.821 5	1.188 2

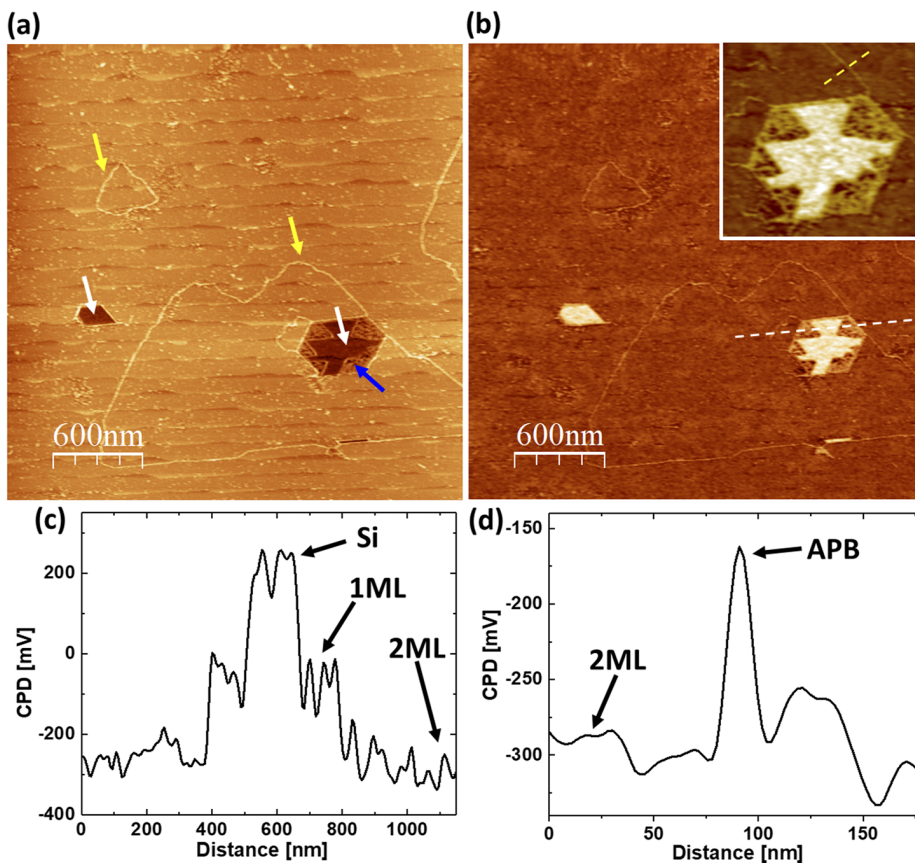


FIG. 7. (a) Topographic ($3 \times 3 \mu\text{m}^2$) nc-AFM image of 2 ml-GaSe film. First GaSe ML (blue arrow) and silicon substrate (white arrows) can be observed on the bottom of the hexagonal pits. APBs are marked with yellow arrows. The z-scale is 1.5 nm (b) corresponding KPFM image (surface potential) with a $700 \times 700 \text{ nm}^2$ image in the inset. APBs appear as positively charged defects with CPD $\sim -160 \text{ mV}$. (c) Cross-section extracted from the KPFM image through 2 ml GaSe film, 1 ml GaSe film and Si substrate [marked with white dotted line on Fig. (b)]. (d) Cross-section extracted from the KPFM image through 2 ml GaSe film and APB [marked with yellow dotted line on Fig. (b)].

in Fig. 7(d). Additionally, we show in Fig. 7(c) the comparison of CPD on 2 ml GaSe and 1 ml GaSe and Si. Similarly to this measurement, the variation of potential depending on the number of layers was reported for other 2D materials.⁷⁵ The work function of the sample ϕ_{sample} can be measured from the relation $V_{\text{CPD}} = (\phi_{\text{tip}} - \phi_{\text{sample}})/e$, where ϕ_{tip} is the work function of the AFM tip and e is the electron charge. ϕ_{tip} is calibrated to be 4.52 eV using a reference sample of annealed highly oriented pyrolytic graphite (HOPG)⁷⁶ with $\phi_{\text{HOPG}} = 4.6 \text{ eV}$. Hence, the work functions are $\phi_{\text{GaSe}(2\text{ml})} = 4.8 \text{ eV}$ and $\phi_{\text{APB}} \sim 4.68 \text{ eV}$. An electron transfer takes place from the defect and the APB is, therefore, positively charged. The band bending in the GaSe film occurs with an energy barrier height of $\Delta\Phi \sim 120\text{--}140 \text{ meV}$ near the APBs. This behavior was observed for all the APBs checked on the sample. Trapping and scattering at these positively charged defects adversely affect the mobility of free-carriers. It is, thus, essential to have a GaSe layer with low APBs density such as the one we managed to grow in this work.

IV. CONCLUSION

In summary, very large-scale growth of 2D-GaSe monolayer on silicon in an industrial MOCVD chamber was demonstrated. The use of a vicinal Si(111) wafer that is slightly misoriented toward

$\langle \bar{1}\bar{1}2 \rangle$ direction allows for a step-edge guided growth of a mainly single-oriented 2D-GaSe crystal. It results in a coalesced film with a very low density of APBs. The APBs are proven to be electrically active in the KPFM measurements; this supports the usefulness of a single-orientation 2D-GaSe film. The screw dislocations formed at the step edges are in large part removed by using an optimized growth-sublimation-regrowth process. This low defectivity GaSe/Si film will serve as an active layer as well as a buffer layer for subsequent growth of more complex vdW heterostructures. This result paves the way for a monolithic cointegration of active 2D materials, and their heterostructures, on silicon chips.

SUPPLEMENTARY MATERIAL

See the [supplementary material](#) for the schematic drawing of the MOCVD tool principle (Fig. S1); (a) AFM images of the GaSe film at different locations along the wafer radius and (b) cross-sectional HAADF-STEM images of the 2 ml-GaSe film at the wafer center and in the middle of the radius (Fig. S2); (a) C1s, (b) Ga3d, (c) Se3d, and (d) Si2p XPS peaks measured at 23.75° with associated fitted data (Fig. S3); and example of the depth profile of elements recalculated from angle resolved spectra (Fig. S4).

ACKNOWLEDGMENTS

This work was partly supported by the French RENATECH network and by the French government managed by ANR under the “investissements d’avenir” economic stimulus package, with Reference Nos. ANR-15-IDEX-02 and ANR-10-EQPX-33 (EQUIPEX IMPACT). The authors want to thank the CEA-Leti cleanroom staff and Jérémie Bissierier for technical assistance on the MOCVD tool. DFT calculations (not shown) were performed using French supercomputers (GENCI) through Project No. 6194.

AUTHOR DECLARATIONS

Conflict of Interest

The authors have no conflicts to disclose.

DATA AVAILABILITY

The data that support the findings of this study are available from the corresponding author upon reasonable request.

REFERENCES

- 1 K. S. Novoselov, A. K. Geim, S. V. Morozov, D. Jiang, Y. Zhang, S. V. Dubonos, I. V. Grigorieva, and A. A. Firsov, *Science* **306**, 666 (2004).
- 2 G. R. Bhimanapati, Z. Lin, V. Meunier, Y. Jung, J. Cha, S. Das, D. Xiao, Y. Son, M. S. Strano, V. R. Cooper, L. Liang, S. G. Louie, E. Ringe, W. Zhou, S. S. Kim, R. R. Naik, B. G. Sumpter, H. Terrones, F. Xia, Y. Wang, J. Zhu, D. Akinwande, N. Alem, J. A. Schuller, R. E. Schaak, M. Terrones, and J. A. Robinson, *ACS Nano* **9**, 11509 (2015).
- 3 S. B. Desai, S. R. Madhvapathy, A. B. Sachid, J. P. Llinas, Q. Wang, G. H. Ahn, G. Pitner, M. J. Kim, J. Bokor, C. Hu, H.-S. P. Wong, and A. Javey, *Science* **354**, 99 (2016).
- 4 O. Lopez-Sanchez, D. Lembke, M. Kayci, A. Radenovic, and A. Kis, *Nat. Nanotechnol.* **8**, 497 (2013).
- 5 H. Zeng, J. Dai, W. Yao, D. Xiao, and X. Cui, *Nat. Nanotechnol.* **7**, 490 (2012).
- 6 A. Segura, J. M. Besson, A. Chevy, and M. S. Martin, *Nuovo Cimento B* **38**, 345 (1977).
- 7 X. Li, M.-W. Lin, J. Lin, B. Huang, A. A. Puzetzy, C. Ma, K. Wang, W. Zhou, S. T. Pantelides, M. Chi, I. Kravchenko, J. Fowlkes, C. M. Rouleau, D. B. Geohegan, and K. Xiao, *Sci. Adv.* **2**, e1501882 (2016).
- 8 P. Hu, Z. Wen, L. Wang, P. Tan, and K. Xiao, *ACS Nano* **6**, 5988 (2012).
- 9 S. Lei, L. Ge, Z. Liu, S. Najmaei, G. Shi, G. You, J. Lou, R. Vajtai, and P. M. Ajayan, *Nano Lett.* **13**, 2777 (2013).
- 10 X. Yuan, L. Tang, S. Liu, P. Wang, Z. Chen, C. Zhang, Y. Liu, W. Wang, Y. Zou, C. Liu, N. Guo, J. Zou, P. Zhou, W. Hu, and F. Xiu, *Nano Lett.* **15**, 3571 (2015).
- 11 R. Lu, J. Liu, H. Luo, V. Chikan, and J. Z. Wu, *Sci. Rep.* **6**, 19161 (2016).
- 12 S. Yang, Q. Yue, H. Cai, K. Wu, C. Jiang, and S. Tongay, *J. Mater. Chem. C* **4**, 248 (2016).
- 13 F. Yan, L. Zhao, A. Patané, P. Hu, X. Wei, W. Luo, D. Zhang, Q. Lv, Q. Feng, C. Shen, K. Chang, L. Eaves, and K. Wang, *Nanotechnology* **28**, 27LT01 (2017).
- 14 Y. Zhou, Y. Nie, Y. Liu, K. Yan, J. Hong, C. Jin, Y. Zhou, J. Yin, Z. Liu, and H. Peng, *ACS Nano* **8**, 1485 (2014).
- 15 Y. Zhou, B. Deng, Y. Zhou, X. Ren, J. Yin, C. Jin, Z. Liu, and H. Peng, *Nano Lett.* **16**, 2103 (2016).
- 16 S. Schwarz, S. Dufferwiel, P. M. Walker, F. Withers, A. A. P. Trichet, M. Sich, F. Li, E. A. Chekhovich, D. N. Borisenko, N. N. Kolesnikov, K. S. Novoselov, M. S. Skolnick, J. M. Smith, D. N. Krizhanovskii, and A. I. Tartakovskii, *Nano Lett.* **14**, 7003 (2014).
- 17 N. Balakrishnan, Z. R. Kudrynskiy, M. W. Fay, G. W. Mudd, S. A. Svatek, O. Makarovskiy, Z. D. Kovalyuk, L. Eaves, P. H. Beton, and A. Patané, *Adv. Opt. Mater.* **2**, 1064 (2014).
- 18 P. Tonndorf, S. Schwarz, J. Kern, I. Niehues, O. Del Pozo-Zamudio, A. I. Dmitriev, A. P. Bakhtinov, D. N. Borisenko, N. N. Kolesnikov, A. I. Tartakovskii, S. Michaelis de Vasconcellos, and R. Bratschitsch, *2D Mater.* **4**, 021010 (2017).
- 19 W. Jie, X. Chen, D. Li, L. Xie, Y. Y. Hui, S. P. Lau, X. Cui, and J. Hao, *Angew. Chem., Int. Ed.* **54**, 1185 (2015).
- 20 X. Zhou, J. Cheng, Y. Zhou, T. Cao, H. Hong, Z. Liao, S. Wu, H. Peng, K. Liu, and D. Yu, *J. Am. Chem. Soc.* **137**, 7994 (2015).
- 21 W. Shi and Y. J. Ding, *Appl. Phys. Lett.* **84**, 1635 (2004).
- 22 W. Shi, Y. J. Ding, N. Ferneliuss, and K. Vodopyanov, *Opt. Lett.* **27**, 1454 (2002).
- 23 V. Nicolosi, M. Chhowalla, M. G. Kanatzidis, M. S. Strano, and J. N. Coleman, *Science* **340**, 1226419 (2013).
- 24 M. Mahjouri-Samani, R. Gresback, M. Tian, K. Wang, A. A. Puzetzy, C. M. Rouleau, G. Eres, I. N. Ivanov, K. Xiao, M. A. McGuire, G. Duscher, and D. B. Geohegan, *Adv. Funct. Mater.* **24**, 6365 (2014).
- 25 Z. Ben Aziza, H. Henck, D. Pierucci, M. G. Silly, E. Lhuillier, G. Patriarche, F. Sirotti, M. Eddrief, and A. Ouergui, *ACS Nano* **10**, 9679 (2016).
- 26 C. H. Lee, S. Krishnamoorthy, D. J. O'Hara, M. R. Brenner, J. M. Johnson, J. S. Jamison, R. C. Myers, R. K. Kawakami, J. Hwang, and S. Rajan, *J. Appl. Phys.* **121**, 094302 (2017).
- 27 M.-W. Chen, H. Kim, D. Ovchinnikov, A. Kuc, T. Heine, O. Renault, and A. Kis, *npj 2D Mater. Appl.* **2**, 2 (2018).
- 28 X. Li, M.-W. Lin, A. A. Puzetzy, J. C. Idrobo, C. Ma, M. Chi, M. Yoon, C. M. Rouleau, I. I. Kravchenko, D. B. Geohegan, and K. Xiao, *Sci. Rep.* **4**, 5497 (2015).
- 29 H. Cai, E. Soignard, C. Ataca, B. Chen, C. Ko, T. Aoki, A. Pant, X. Meng, S. Yang, J. Grossman, F. D. Ogletree, and S. Tongay, *Adv. Mater.* **28**, 7375 (2016).
- 30 T. Afaneh, A. Fryer, Y. Xin, R. H. Hyde, N. Kapuruge, and H. R. Gutiérrez, *ACS Appl. Nano Mater.* **3**, 7879 (2020).
- 31 S. M. Eichfeld, L. Hossain, Y.-C. Lin, A. F. Piasecki, B. Kupp, A. G. Birdwell, R. A. Burke, N. Lu, X. Peng, J. Li, A. Azcatl, S. McDonnell, R. M. Wallace, M. J. Kim, T. S. Mayer, J. M. Redwing, and J. A. Robinson, *ACS Nano* **9**, 2080 (2015).
- 32 S. M. Eichfeld, V. O. Colon, Y. Nie, K. Cho, and J. A. Robinson, *2D Mater.* **3**, 025015 (2016).
- 33 Y.-C. Lin, B. Jariwala, B. M. Bersch, K. Xu, Y. Nie, B. Wang, S. M. Eichfeld, X. Zhang, T. H. Choudhury, Y. Pan, R. Addou, C. M. Smyth, J. Li, K. Zhang, M. A. Haque, S. Fölsch, R. M. Feenstra, R. M. Wallace, K. Cho, S. K. Fullerton-Shirey, J. M. Redwing, and J. A. Robinson, *ACS Nano* **12**, 965 (2018).
- 34 X. Zhang, T. H. Choudhury, M. Chubarov, Y. Xiang, B. Jariwala, F. Zhang, N. Alem, G.-C. Wang, J. A. Robinson, and J. M. Redwing, *Nano Lett.* **18**, 1049 (2018).
- 35 K. Kang, S. Xie, L. Huang, Y. Han, P. Y. Huang, K. F. Mak, C.-J. Kim, D. Muller, and J. Park, *Nature* **520**, 656 (2015).
- 36 T. Kim, J. Mun, H. Park, D. Joung, M. Diware, C. Won, J. Park, S.-H. Jeong, and S.-W. Kang, *Nanotechnology* **28**, 18LT01 (2017).
- 37 G. Siegel, G. Gryzbowski, A. Hilton, C. Muratore, and M. Snure, *Crystals* **9**, 339 (2019).
- 38 X. Li, S. Sundaram, Y. El Gmili, T. Ayari, R. Puybaret, G. Patriarche, P. L. Voss, J. P. Salvestrini, and A. Ougazzaden, *Cryst. Growth Des.* **16**, 3409 (2016).
- 39 H. Jeong, D. Y. Kim, J. Kim, S. Moon, N. Han, S. H. Lee, O. F. N. Okello, K. Song, S.-Y. Choi, and J. K. Kim, *Sci. Rep.* **9**, 5736 (2019).
- 40 T. H. Choudhury, H. Simchi, R. Boichot, M. Chubarov, S. E. Mohney, and J. M. Redwing, *Cryst. Growth Des.* **18**, 4357 (2018).
- 41 X. Zhang, F. Zhang, Y. Wang, D. S. Schulman, T. Zhang, A. Bansal, N. Alem, S. Das, V. H. Crespi, M. Terrones, and J. M. Redwing, *ACS Nano* **13**, 3341 (2019).
- 42 R. Yue, Y. Nie, L. A. Walsh, R. Addou, C. Liang, N. Lu, A. T. Barton, H. Zhu, Z. Che, D. Barrera, L. Cheng, P.-R. Cha, Y. J. Chabal, J. W. P. Hsu, J. Kim, M. J. Kim, L. Colombo, R. M. Wallace, K. Cho, and C. L. Hinkle, *2D Mater.* **4**, 045019 (2017).
- 43 D. Dumcenco, D. Ovchinnikov, K. Marinov, P. Lazić, M. Gibertini, N. Marzari, O. L. Sanchez, Y.-C. Kung, D. Krasnozhan, M.-W. Chen, S. Bertolazzi, P. Gillet, A. Fontcuberta i Morral, A. Radenovic, and A. Kis, *ACS Nano* **9**, 4611 (2015).
- 44 H. Yu, M. Liao, W. Zhao, G. Liu, X. J. Zhou, Z. Wei, X. Xu, K. Liu, Z. Hu, K. Deng, S. Zhou, J.-A. Shi, L. Gu, C. Shen, T. Zhang, L. Du, L. Xie, J. Zhu, W. Chen, R. Yang, D. Shi, and G. Zhang, *ACS Nano* **11**, 12001 (2017).

- ⁴⁵X. Liu, I. Balla, H. Bergeron, G. P. Campbell, M. J. Bedzyk, and M. C. Hersam, *ACS Nano* **10**, 1067 (2016).
- ⁴⁶A. M. van der Zande, P. Y. Huang, D. A. Chenet, T. C. Berkelbach, Y. You, G.-H. Lee, T. F. Heinz, D. R. Reichman, D. A. Muller, and J. C. Hone, *Nat. Mater.* **12**, 554 (2013).
- ⁴⁷T. H. Ly, D. J. Perello, J. Zhao, Q. Deng, H. Kim, G. H. Han, S. H. Chae, H. Y. Jeong, and Y. H. Lee, *Nat. Commun.* **7**, 10426 (2016).
- ⁴⁸O. V. Yazayev and Y. P. Chen, *Nat. Nanotechnol.* **9**, 755 (2014).
- ⁴⁹L. Chen, B. Liu, M. Ge, Y. Ma, A. N. Abbas, and C. Zhou, *ACS Nano* **9**, 8368 (2015).
- ⁵⁰L. Wang, X. Xu, L. Zhang, R. Qiao, M. Wu, Z. Wang, S. Zhang, J. Liang, Z. Zhang, Z. Zhang, W. Chen, X. Xie, J. Zong, Y. Shan, Y. Guo, M. Willinger, H. Wu, Q. Li, W. Wang, P. Gao, S. Wu, Y. Zhang, Y. Jiang, D. Yu, E. Wang, X. Bai, Z.-J. Wang, F. Ding, and K. Liu, *Nature* **570**, 91 (2019).
- ⁵¹L. Zhang, P. Peng, and F. Ding, *Adv. Funct. Mater.* **31**, 2100503 (2021).
- ⁵²R. Fritsche, E. Wisotzki, A. B. M. O. Islam, A. Thissen, A. Klein, W. Jaegermann, R. Rudolph, D. Tonti, and C. Pettenkofer, *Appl. Phys. Lett.* **80**, 1388 (2002).
- ⁵³R. Fritsche, E. Wisotzki, A. Thißen, A. B. M. O. Islam, A. Klein, W. Jaegermann, R. Rudolph, D. Tonti, and C. Pettenkofer, *Surf. Sci.* **515**, 296 (2002).
- ⁵⁴T. Ohta, A. Klust, J. A. Adams, Q. Yu, M. A. Olmstead, and F. S. Ohuchi, *Phys. Rev. B* **69**, 125322 (2004).
- ⁵⁵R. Rudolph, C. Pettenkofer, A. A. Bostwick, J. A. Adams, F. Ohuchi, M. A. Olmstead, B. Jaeckel, A. Klein, and W. Jaegermann, *New J. Phys.* **7**, 108 (2005).
- ⁵⁶A. Ohtake and Y. Sakuma, *Appl. Phys. Lett.* **114**, 053106 (2019).
- ⁵⁷M. A. Olmstead and F. S. Ohuchi, *J. Vac. Sci. Technol., A* **39**, 020801 (2021).
- ⁵⁸W. Zhao, M. Steidl, A. Paszuk, S. Brückner, A. Dobrich, O. Supplie, P. Kleinschmidt, and T. Hannappel, *Appl. Surf. Sci.* **392**, 1043 (2017).
- ⁵⁹Y. Sugawara, L. Kou, Z. Ma, T. Kamijo, Y. Naitoh, and Y. Jun Li, *Appl. Phys. Lett.* **100**, 223104 (2012).
- ⁶⁰B. Pelissier, H. Kambara, E. Godot, E. Veran, V. Loup, and O. Joubert, *Microelectron. Eng.* **85**, 151 (2008).
- ⁶¹B. Pelissier, S. Labau, M. Martin, C. Petit-Etienne, H. Fontaine, T. Baron, and O. Joubert, *Microelectron. Eng.* **231**, 111401 (2020).
- ⁶²R. Chen, J. Cao, S. Gee, Y. Liu, and J. Yao, *MRS Adv.* **5**, 3437 (2020).
- ⁶³R. L. Schwoebel and E. J. Shipsey, *J. Appl. Phys.* **37**, 3682 (1966).
- ⁶⁴G. Ehrlich and F. G. Hudda, *J. Chem. Phys.* **44**, 1039 (1966).
- ⁶⁵G. D. T. Spiller, M. Hanbucken, and J. A. Venables, *Rep. Prog. Phys.* **47**, 399 (1984).
- ⁶⁶M. Dai, Y. Wang, J. Kwon, M. D. Halls, and Y. J. Chabal, *Nat. Mater.* **8**, 825 (2009).
- ⁶⁷O. Supplie, O. Romanyuk, C. Koppka, M. Steidl, A. Nägelein, A. Paszuk, L. Winterfeld, A. Dobrich, P. Kleinschmidt, E. Runge, and T. Hannappel, *Prog. Cryst. Growth Charact. Mater.* **64**, 103 (2018).
- ⁶⁸R. Kawaguchi, T. Eguchi, and S. Suto, *Surf. Sci.* **686**, 52 (2019).
- ⁶⁹K. Ueno, N. Takeda, K. Sasaki, and A. Koma, *Appl. Surf. Sci.* **113–114**, 38 (1997).
- ⁷⁰X. Li, J. Dong, J. C. Idrobo, A. A. Puzos, C. M. Rouleau, D. B. Geohegan, F. Ding, and K. Xiao, *J. Am. Chem. Soc.* **139**, 482 (2017).
- ⁷¹J. F. Moulder, W. F. Stickle, P. E. Sobol, and K. D. Bomben, *Handbook of X-Ray Photoelectron Spectroscopy* (Physical Electronics Inc., Eden Prairie, MN, 1995), p. 41.
- ⁷²S. Tanuma, C. J. Powell, and D. R. Penn, *Surf. Interface Anal.* **43**, 689 (2011).
- ⁷³P. J. Cumpson and M. P. Seah, *Surf. Interface Anal.* **18**, 345 (1992).
- ⁷⁴J. M. Thomas, I. Adams, R. H. Williams, and M. Barber, *J. Chem. Soc., Faraday Trans. 2* **68**, 755 (1972).
- ⁷⁵S. J. Sque, R. Jones, and P. R. Briddon, *Phys. Status Solidi* **204**, 3078 (2007).
- ⁷⁶P. A. F. Garrillo, B. Grévin, N. Chevalier, and L. Borowik, *Rev. Sci. Instrum.* **8**, 661 (2018).